A Computational Study of Particle Deposition Patterns from a Circular Laminar Jet

J. Q. Feng

Optomec, Inc., 2575 University Avenue, #135, St. Paul, Minnesota, 55114, USA

Email: jfeng@optomec.com

ABSTRACT

To gain insights into ink material deposition behavior during Aerosol Jet® printing, particle deposition patterns on the plate of inertial impactor with circular laminar jet are investigated numerically with a lagrangian solver implemented within the framework of the OpenFOAM® CFD package. Effects of taper angle of the nozzle channel and jet-to-plate distance are evaluated. The results show quite different particle deposition patterns between tapered nozzle and straight nozzle. At jet Reynolds number Re = 1132, a tapered nozzle deposits particles to form a pattern with a high density ring toward the deposition spot edge, especially when the particle Stokes number $St > St_{50}$, which is absent with a straight nozzle. Increasing the jet-to-plate distance tends to reduce such particle density peak. Reducing Re to 283 yields particle deposition patterns without the high density ring near the spot edge, with the same tapered nozzle. The particle deposition patterns with the straight nozzle at Re = 283 exhibit further reduced particle density around the spot edge such that the particle density profile appears more like a Gaussian function. In general, the effect of reducing Re on particle deposition pattern seems to be similar to increasing the jet-to-plate distance. The computed particle deposition efficiency η shows the fact that those particles around the jet axis, even with very small values of St, always impact the center of plate, as indicated by the nonvanishing value of η with substantial reduction of St. Such a "small particle contamination" typically amounts to ~10% of small particles (with $\sqrt{St}$ < 0.1) at Re ~ 1000 and ~5% at Re ~ 300, which may not be negligible in data analysis with inertial impactor measurement.

Keywords: Particle deposition; Laminar jet; Inertial impactor; Aerosol Jet®; Computational analysis.

NOMENCLATURE

C_c	Cuningham slip correction factor	$\bar{r}$	radial position on impaction plate
D	circular orifice diameter of nozzle	Re	jet Reynolds number ($=\rho\,U\,D\,/\,\mu$)
D_{in}	inlet diameter of nozzle channel	S	jet-to-plate distance
d_p	particle diameter	St	Stokes number [$=\rho_p\,U\,C_c\,d_p^2\,/\,(9\,\mu\,D)$]
η	particle deposition efficiency	St_{50}	value of St for η = 50%
L_s	particle stop distance	σ	(dimensionless) surface mass density
μ	viscosity of carrier gas	T	nozzle throat length
Q	volumetric gas flow rate	τ	particle relaxation time
ρ	density of carrier gas	U	average velocity of laminar jet
ρ_p	density of particle		
r	radial position on impaction plate	ϕ	half angle of tapering section
$\hat{r}$	radial position on impaction plate		

1. INTRODUCTION

Many authors have studied particle impaction behavior with circular jets, mainly for its application in aerosol particle classification by aerodynamic size with the cascade impactors (e.g., Anderson, 1966; Marple and Willeke, 1976; Hering, 1995). The original inertial impaction theory was presented by Ranz and Wong (1952). Practical designs of the inertial impactors have been

guided by numerically computing the flow field governed by the Navier-Stokes equations and then integrating equations governing the particle motions for analysis of particle trajectories (cf. Marple, 1970; Marple and Liu, 1974; Huang and Tsai, 2001). Based on a thorough parametric study, Marple (1970); Marple and Liu (1974, 1975) found that relatively sharp cutoff deposition efficiency curves can be obtained when the jet Reynolds number is between 500 and 3000. The gravity effect on collection efficiency of large particles in the low-velocity inertial impactor was demonstrated experimentally by May (1975). Both numerical and experimental studies of the gravity effect on particle collection efficiency in inertial impactors were carried out by Huang and Tsai (2001). However, the study of particle deposition patterns with circular laminar jet could only be found in a publication by Sethi and John (1993) with laboratory experiments for one geometric configuration.

With the Aerosol Jet® direct-write technology, functional ink is aerosolized via a liquid atomizer and transported as a dense mist of microdroplets (usually about 50 nL/cc), through a nozzle with a small orifice and deposited onto the substrate by the mechanism of inertial impaction with an impinging jet (cf. Renn, 2006, 2007; Renn *et al*., 2009). It enables precision high-aspect-ratio material deposition for a variety of scientific and industrial applications (cf. Hedges, 2007; Kahn, 2007; Renn *et al*., 2010; Christenson *et al*., 2011; Paulsen *et al*. 2012). For well-controlled high-precision material deposition, the mist flow impacting on substrate is maintained in the steady laminar regime for Aerosol Jet ® printing. An in-depth understanding the basic deposition behavior of microdroplets (typically with diameters of a few microns) with a circular laminar jet is important for Aerosol Jet® deposition nozzle design as well as process development.

In the present work, a method for evaluating particle deposition patterns is developed with computational analysis using a lagrangian solver implemented within the framework of OpenFOAM® CFD package (www.openfoam.com). In what follows, the computational methodology is presented in section 2, and then results and discussion in section 3 for cases of straight nozzle ($\phi = 0$) and tapered nozzle ($\phi = 15°$). Finally, the conclusions are summarized in section 4.

2. COMPUTATIONAL METHOD

As schematically shown in Fig. 1, the inertial impactor consists of a nozzle with an circular orifice of diameter D and an impaction plate of much larger diameter located at a "jet-to-plate" distance S. Moreover, geometric parameters such as nozzle throat length T, half angle of the tapering section ϕ, etc. can also influence the particle impaction behavior. With a given geometric configuration, the particle-laden mist flow may be generally assumed as incompressible (with the flow velocity much less than the speed of sound),

laminar (with jet Reynolds number less than 1500, cf. Marple, 1970; Marple and Liu, 1974, 1975), and steady (with the jet-to-plate distance S comparable to D). Thus, the flow field is governed by the continuity equation for incompressible flow

$$\nabla \cdot u = 0 \tag{1}$$

and steady flow momentum equation (also known as the Navier-Stokes equations for steady flow)

$$\nabla \cdot (uu) + \nabla \cdot (v\nabla u) = -\nabla p \tag{2}$$

where u is the vector field of flow velocity and p the kinematic pressure (which comes from the thermodynamic pressure divided by the constant fluid density of the carrier gas ρ), with v denoting the (constant) kinematic viscosity of the carrier gas (assuming the particles are not too dense to alter the fluid viscosity, which is usually reasonable with the mist used in Aerosol Jet® printing).
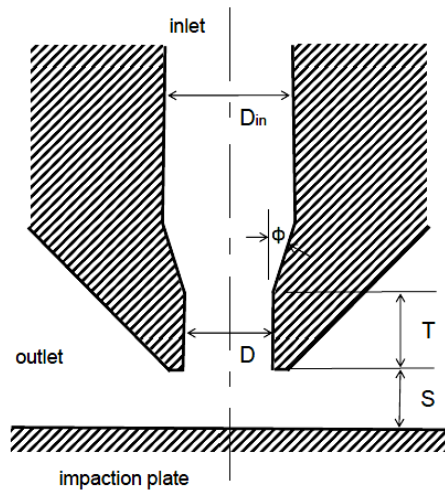

Fig. 1. Schematic of the circular-jet impactor geometric configuration.

The solution of flow field governed by (1) and (2) can be computed with the simpleFoam solver (implemented for steady incompressible flow using the SIMPLE algorithm) in the OpenFOAM® CFD package. If length is measured in units of the nozzle orifice diameter D, velocity u in units of $U = 4 Q / (\pi D^2)$ with Q denoting the volumetric flow rate entering the impactor, and kinematic pressure p in units of U^2, the nondimensionalized (2) would have n replaced by $1/Re$ where the jet Reynolds number Re is defined as

$$Re = \frac{UD}{v} = \frac{\rho UD}{\mu} \tag{3}$$

with μ denoting the dynamic viscosity of the carrier gas. For the present problem (cf. Fig. 1), there are three types of boundaries: inlet, outlet, and walls. The boundary conditions at inlet are simply the *zero Gradient* type for p (namely, $n \cdot \nabla p = 0$) and the *flow Rate Inlet Velocity* type with a specified volumetric flow rate Q for u, which is equivalent to having a plug flow at the inlet as if the flow is

coming from a large upstream open volume. At outlet, the *fixed Value* type for p (= 0) and the *zero Gradient* type for u (namely, $nn : \nabla u = 0$) are applied; and at walls, the *zero Gradient* type for p and the *fixed Value* type for u (=0) are used.

Once the flow velocity field u is computed, the position vector of each particle x_p in a Lagrangian frame can be determined from the equations of motion

$$\frac{dx_p}{dt} = u_p \qquad (4)$$

and

$$m_p \frac{du_p}{dt} = \sum f_p \qquad (5)$$

where u_p denotes the particle velocity at position x_p and time t, m_p the particle mass, and f_p the forces acting on the particle. The OpenFOAM® CFD package contains a *basic Kinematic Cloud* class to introduce kinematic parcels and to track the parcel positions according to the specified forces $\sum f_p$. In general, a parcel is a computational particle, which may contain multiple actual particles depending upon the model specifications, to reduce the computational burden for tracking large number of individual particles. When the number of particles is not large, a parcel can be computed as an individual actual particle (as in the present work).

For Aerosol Jet® printing, the mist of ink droplets usually contains ink of about 50 nL/cc, or with a ink volume fraction of 5×10^{-5}. Thus, the ink droplets can be considered far enough apart that each droplet behave as an isolated spherical particle in the mist flow. Because the ink droplets suitable for Aerosol Jet® printing typically have diameters in the range of 1 to 5 μm, Brownian diffusion effect (which usually becomes important for particles smaller than 0.5 μm, cf. Fuchs, 1964; Friedlander, 1977) should be negligible. Thus, the dominant forces acting on each particle are the viscous drag f_d due to the relative motion in fluid and the gravitational force m_p g, i.e., $\sum f_p = f_d + \pi \rho_p d_p^3 g / 6$ (with ρ_p denoting the particle density, d_p the particle diameter, and g = 9.81 m s^{-2} the gravitational acceleration in the jet flow direction). In the present work, the particles are assumed to be spheres to represent ink droplets; thus, the *sphere Drag* and *gravity* are specified as the *particle Forces* in the *kinematic Cloud Properties*. In OpenFOAM-2.4.0 (which is used in the present work), the sphere drag f_d is computed according to

$$f_d = \frac{\pi \mu d_p}{8} C_d \, \mathrm{Re}_p \left(u - u_p \right) \qquad (6)$$

where the drag coefficient C_d is calculated by

$$C_d = \frac{24}{\mathrm{Re}_p} \left(1 + \frac{1}{6} \mathrm{Re}_p^{2/3} \right) \text{ for } \mathrm{Re}_p \leq 1000 \qquad (7)$$

and C_d = 0.424 if Re_p > 1000 (which seems to be

slightly modified from that given by Schiller and Naumann, 1933), with the particle Reynolds number defined as

$$\mathrm{Re}_p \equiv \frac{d_p |u - u_p|}{\nu} = \frac{\rho d_p |u - u_p|}{\mu} \quad . \qquad (8)$$

To keep the model theoretically clean, a lagrangian solver is implemented within the OpenFOAM® framework such that the presence of kinematic cloud parcels does not disturb the given steady flow field obtained from the *simple Foam* computations, while the motion of parcels is determined by solving (4)-(6) from the given flow field u. It should be noted that (6) in the OpenFOAM® implementation does not contain the Cunningham slip correction factor C_c in the denominator as usually seen in the aerosol science literature. Therefore, it is added in by modifying the source code of *SphereDragForce.C* to replace μ by μ / C_c with

$$C_c = 1 + \frac{\lambda}{d_p} \left[A_1 + A_2 \exp\left(\frac{-A_3 d_p}{\lambda} \right) \right] \qquad (9)$$

where λ is the mean free path of the gas (which is about 0.065 μm at 25º C) with A_1 = 2.514, A_2 = 0.8, and A_3 = 0.55 (Friedlander, 1977).

With the OpenFOAM® lagrangian solver, particles can be introduced in flow by several built-in *injection Models*, among which the type of *manual Injection* allows particles (one per parcel) of specified diameter to be injected at specified positions inside problem domain. In the present work, a set of particles of identical properties is placed near the flow inlet at known radial positions from the axis of symmetry with given spacing, e.g., $\hat{r} = i \times \Delta \hat{r}$ with i = 0, 1, 2, …, with the particle initial velocity specified to match that of the inlet plug flow. The radial positions of individual particles on the impaction plate r_i can be extracted from the *patch Post Processing* data file. Then, assuming the particle concentration is uniform at the nozzle inlet, a dimensionless surface mass density of deposited particles σ at a given radial position r_i on the impaction plate can be calculated as

$$\sigma = \frac{\hat{r}_{i+1} - \hat{r}_{i-1}}{r_{i+1} - r_{i-1}} \text{ for } i \neq 0 \text{ and } \sigma_0 = 2\sigma_1 - \sigma_2. \quad (10)$$

Noteworthy here is that the density of deposited particles on the impaction plate σ given by (10) is inversely proportional to the change of relative spacing between neighboring particles, with $\hat{r}_i$ and r_i denoting the beginning (at the inlet) and ending (at the impaction plate) positions of the trajectory of particle i. The number of particles arriving the impaction plate within the ring defined by r_{i-1} and r_{i+1} is expected to be conserved, i.e., being the same as that at inlet with plug flow within the ring defined by $\hat{r}_{i-1}$ and $\hat{r}_{i+1}$ from the inlet.

For a given d_p, there is a critical radius $\hat{r}_c$ ($\leq D_{in}/2$)

at the nozzle inlet beyond which the particles could not be deposited on the impaction plate; they exit through the outlet boundary. Because the particle concentration and flow velocity profile are assumed to be uniform at the inlet (as consistent with the specified plug flow boundary condition), the particle deposition efficiency can be simply determined as an area ratio

$$\eta = \left(\frac{2\hat{r}_c}{D_{in}} \right) \qquad (11)$$

where D_{in} is the diameter of nozzle inlet (Fig. 1).

The value of the particle Stokes number St, defined as the ratio of the particle stopping distance and the radius of the nozzle orifice ($D/2$), can be written as (Fuchs, 1964)

$$St = \frac{\rho_p U C_c d_p^{\,2}}{9 \mu D} \qquad . \qquad (12)$$

In the literature of inertial impactors, curves are usually presented in terms of the particle deposition efficiency η versus $\sqrt{St}$, where $\sqrt{St}$ is often considered as the dimensionless particle diameter.

With the OpenFOAM® *basic Kinematic Cloud* class, several interaction models between parcel and boundary patch are available. Although particle rebound can be modeled with appropriately specified elasticity and restitution coefficient, it is much simpler to just assume the particle remains where it contacts the surface. Here, the mode of local interactions between particles and boundary patches is simply specified as *stick* in the *kinematic Cloud Properties* dictionary file, which is especially reasonable for Aerosol Jet® printing, because the particles are actually the liquid microdroplets of ink materials. Thus, droplet rebounding and splashing are not considered in the computation, for simplicity.

3. RESULTS AND DISCUSSION

For convenience of comparison, the nominal settings in the geometric configuration shown in Fig. 1 (similar to that used by Sethi and John, 1993) are $D = 1.5$ mm, $T/D = 2.0$, with various S/D and ϕ. The jet Reynolds number Re can be varied by changing the volumetric flow rate Q specified at the inlet. For the carrier gas, μ is taken as 1.8×10^{-5} N s m^{-2} and ρ as 1.2 kg m^{-3}, as typical values for nitrogen under ambient condition. Thus, we have $Re = 1132$ for $Q = 1200$ ccm with $U = 4 Q / (\pi D^2) = 11.3$ m s^{-1}. The value of particle density ρ_p is assumed to be 10^3 kg m^{-3}; therefore, the spherical particle diameter d_p is the same as the "aerodynamic diameter".

Full three-dimensional mesh is used here such that the particles can be placed with adequate spacing in between, to avoid particle-particle interactions in the *basic Kinematic Cloud* class. Fig. 2 shows the streamline plot of the *simple Foam* solution for the geometric configuration of $S/D = 1$, $T/D = 2$, and

$\phi = 15^\circ$, along with the 3D mesh used for the computation. The *block Mesh* utility of OpenFOAM® is used for generating high-quality hexahedral mesh with finite-volume cells in the nozzle and impaction regions being around 70 μm, which is adequate for accurately resolving the laminar flow field of impinging jet while being much larger than the particle diameter as desired for lagrangian tracking of discrete particles. The steady jet impinging flow structure appears fairly similar to that shown for $Re = 1000$ in an independent study with a different computational methodology by Feng (2015).
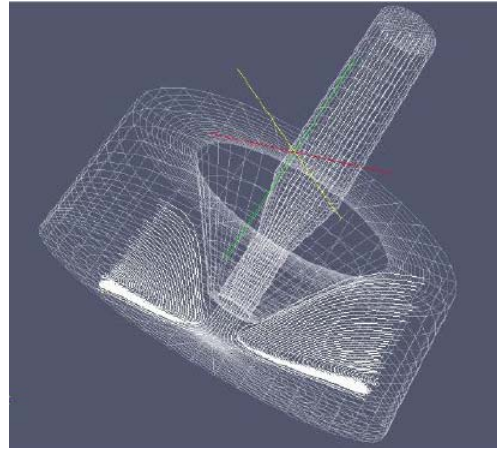

Fig. 2. Streamlines of flow in a circular-jet impactor for Re = 1132 with D = 1.5 mm and D_{in} = 3 mm, S/D = 1, T/D = 2, and ϕ=15°. The mesh of problem domain generated with *block Mesh* is also shown. The outlet boundary is at radius equal to 5x*D*.

For reference, Table 1 illustrates the values of St and $\sqrt{St}$, along with the particle motion parameters such as characteristic time (or relaxation time) of particles in response to nonuniform rectilinear flow $\tau = St\, D/(2U)$ and stop distance $L_s = St\, D/2$, for various particle diameter d_p at $Re = 1132$ with $D = 1.5$ mm. Because $U > 10$ m/s and the value of Froude number $Fr = U^2/(g\, D)$ is greater than 6795, the effect of gravity is expected negligible according to Huang and Tsai (2001), although gravity is included in the OpenFOAM® code by default in Eq. (6).

Although S is often comparable to D in typical impactors for particle size analysis, much larger values of S/D (e.g., ~10) is usually employed in the nozzle-to-plate settings with Aerosol Jet® printing. Therefore, the present study examines a range of S/D from 0.5 to 4 for providing insights into both traditional inertial impactor and Aerosol Jet® applications.

3.1 Straight Nozzle Without Taper ($\phi = 0$)

The case without nozzle channel taper represents the simplest geometric configuration for computational modeling. It is especially of theoretical importance because aerosol flow in the

nozzle channel is better defined.

Table 1 The values of *St*, $\sqrt{St}$, τ (ms), L_s (mm) for various d_p at *Re* = 1132 with *D* = 1.5 mm

d_p (mm)	*St*	$\sqrt{St}$	τ (ms)	L_s (mm)
0.5	0.016	0.124	0.0010	0.012
1	0.054	0.233	0.0036	0.041
1.5	0.116	0.341	0.0077	0.087
1.75	0.156	0.395	0.0103	0.117
2	0.202	0.449	0.0134	0.151
3	0.442	0.665	0.0293	0.332
4	0.776	0.881	0.0514	0.582
5	1.202	1.097	0.0797	0.902
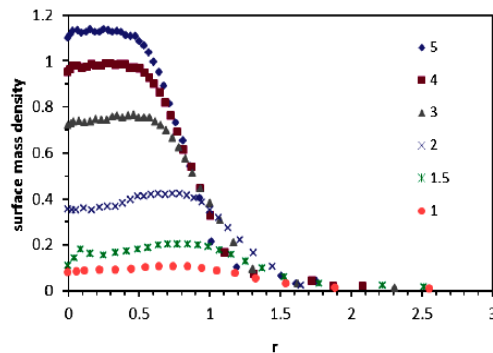
Fig. 3. The dimensionless surface mass density σ as a function of normalized radial position *r* (in units of *D*/2 = 0.75 mm) on the impaction plate for *Re* = 1132 with *D* = 1.5 mm, *S/D* = 1, *T/D* = 2, and ϕ=0°. The labels are the values of particle diameter d_p in units of *μ*m, with corresponding values of $\sqrt{St}$ = 1.097, 0.881, 0.665, 0.449, 0.341, and 0.233 as given in Table 1.

Figure 3 shows particle deposition patterns in terms of the dimensionless surface density σ as a function of the normalized radial position *r* on the impaction plate, determined according to (10). In this case, the jet Reynolds number Re is 1132 (for a flow rate of *Q* = 1200 ccm though a nozzle of *D* = 1.5 mm). With particle density of ρ_p = 1000 kg m^{-3}, the particles of diameter d_p in a range of 0.5 to 5 *μ*m cover the range of $\sqrt{St}$ from 0.124 to 1.097 (cf. Table 1), wherein most significant variation of the particle deposition efficiency *η* is expected. Obviously, fewer particles of smaller size could be deposited on the impaction plate; therefore, we have relatively lower surface mass density σ for smaller $\sqrt{St}$. It is interesting to note that the particle deposition pattern σ(*r*) also changes with d_p (or $\sqrt{St}$). Smaller particles tends to have slightly lower deposition rate at the center (around *r* = 0) with higher deposition rate extending to larger radial position *r*. For larger particles such as d_p = 4 and 5 *μ*m (or $\sqrt{St}$ = 0.881 and 1.097), the values of

deposition efficiency are both *η* = 100% (cf. Table 2) but the particle deposition patterns exhibit noticeable differences. The profile of d_p = 4 *μ*m is about 10% lower than that of d_p = 5 *μ*m in the middle region (r < 1), but becomes higher at larger radial distance (r > 1) such that the two different profiles correspond to the same amount of (normalized) particle volume on the impaction plate.

Table 2 The values of impaction efficiency *η* versus $\sqrt{St}$ for *S/D* = 0.5, 1, 2, and 4 (as the subscript of *η*) at *Re* = 1132 with *D* = 1.5 mm and ϕ=0° (straight nozzle). The values of $\sqrt{St_{50}}$ (corresponding to *η* = 0.5) are 0.389, 0.346, 0.351, and 0.362 for *S/D* = 0.5, 1, 2, and 4, respectively

$\sqrt{St}$	$\eta_{0.5}$	η_1	η_2	η_4
0.124	0.09	0.17	0.17	0.19
0.233	0.14	0.26	0.27	0.27
0.341	0.32	0.49	0.48	0.46
0.395	0.52	0.63	0.61	0.57
0.449	0.71	0.76	0.73	0.69
0.665	0.93	0.94	0.94	0.94
0.881	0.98	1.00	1.00	1.00
1.097	1.00	1.00	1.00	1.00

Because the particle deposition patterns typically exhibit a rapid declining edge followed by a rather long tail with insignificant particle density, it may be meaningful to use the radial position for σ to reach half of its peak value (where the slope is expected to be close to its maximum magnitude as can be easily determined in profilometer measurements) to define the deposition spot size, such as the "spot radius" $\bar{r}$ or "spot diameter" $\bar{d} = 2\bar{r}$. For example, the cases of d_p = 5 μm ($\sqrt{St}$ = 1.097) and d_p = 3 μm ($\sqrt{St}$=0.665) in Fig. 3 have $\bar{r}$ = 0.79 and 0.93, respectively (both are < 1, i.e., less than the nozzle radius). But for d_p = 2 μm ($\sqrt{St}$ = 0.449) and d_p = 1 μm ($\sqrt{St}$=0.233), the spot radius would become $\bar{r}$ = 1.19 and 1.24, respectively (both larger than the nozzle radius). It is understandable that the particle deposition pattern spreads out as indicated by the increasing value of $\bar{r}$ with reducing $\sqrt{St}$, because the smaller particles tend to follow the deflecting streamlines of gas flow more closely. Interestingly though, the value of $\bar{r}$ is 1.21 for the case of d_p = 0.5 μm ($\sqrt{St}$=0.124, not shown in Fig. 3). The reason for a shrinking $\bar{r}$ with further reducing $\sqrt{St}$ is that particles located in the outer rings further away from the axis are unable to contact the plate, being carried by the deflecting gas flow to the outlet.
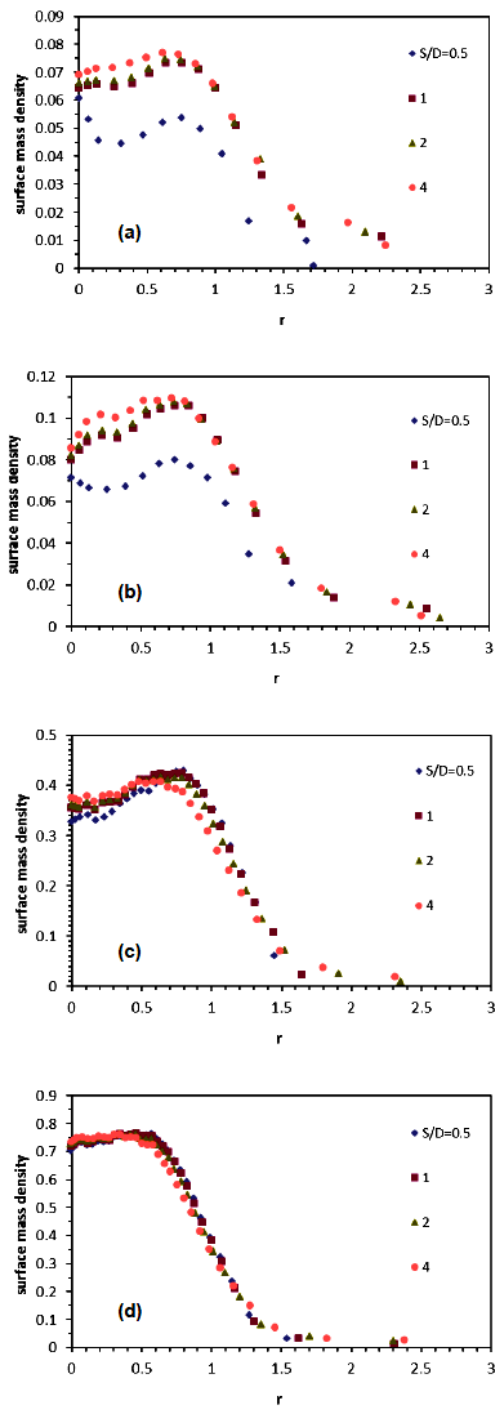
Fig. 4. As in Fig. 3 but with S/D = 0.5, 1, 2, and 4 as labeled. Plot (a) is for d_p = 0.5 μm, (b) d_p = 1 μm, (c) d_p = 2 μm, and (d) d_p = 3 μm.

Figure 4 shows the effects of varying the (normalized) jet-to-plate distance S/D with the straight nozzle at Re = 1132 for (a) $\sqrt{St}$ = 0.124, (b) 0.233, (c) 0.449, and (d) 0.665. The deposition pattern varies considerably with changing S/D from 0.5 to 4 for small particles with $\sqrt{St}$ < 0.4, but becomes relatively insensitive to S/D when $\sqrt{St}$ is greater than 0.5. The change in particle deposition pattern is mostly noticeable when S/D varies

between 0.5 and 1, especially for small $\sqrt{St}$, but not much so for S/D > 1. The values of spot radius $\bar{r}$ in Fig. 4(a) with $\sqrt{St}$ = 0.124 are 1.16, 1.21, 1.21, and 1.20, respectively for S/D = 0.5, 1, 2, and 4, whereas that in Fig. 4(b) for $\sqrt{St}$ = 0.233 become $\bar{r}$ = 1.16, 1.24, 1.24, and 1.24. The spot radius tends to increase somewhat, mostly when S/D changes from 0.5 to 1 (for small $\sqrt{St}$). However, for the case of larger $\sqrt{St}$ as in Fig. 4(c) with $\sqrt{St}$ = 0.449, we have $\bar{r}$ = 1.20, 1.19, 1.19, and 1.15, (respectively for S/D = 0.5, 1, 2, and 4). Similarly, the case of Fig. 4(d) with $\sqrt{St}$ = 0.665 has $\bar{r}$ = 0.95, 0.93, 0.91, and 0.89, exhibiting a trend of slight decrease in the spot radius with increasing S/D (for larger $\sqrt{St}$).

Table 2 shows computed deposition efficiency η for various $\sqrt{St}$ (corresponding to d_p = 0.5, 1, 1.5, 1.75, 2, 3, 4, and 5 **μm**) with the value of S/D, e.g., 0.5, 1, 2, and 4, labeled as the subscript. Again, the change in η is mostly noticeable when S/D varies from 0.5 to 1, especially when $\sqrt{St}$ < 0.4, but not much so for S/D > 1. It is a bit counterintuitive to see that the deposition efficiency for a given $\sqrt{St}$ tends to be lower for S/D = 0.5, namely, when the impaction plate is closer to the nozzle exit, especially for small particles. This could be a result of sharper bend of the deflecting gas flow with shorter impinging jet (at smaller S/D) that enables more effective removal of small particles. But this also indicates a sharper cut for the particle deposition efficiency as a function of particle size, with an impactor having smaller S/D. Increasing the jet-to-plate distance S/D would lead to a more gradual change of η versus $\sqrt{St}$ especially for relatively small $\sqrt{St}$. The value of $\sqrt{St_{50}}$ though is rather insensitive to the change of S/D (from 0.5 to 4), varying within 10% from the average value of 0.362 with a minimum of 0.346 around S/D = 1.

Another observation from Table 2 is that significant amount of particle deposition still occurs (e.g., with η ~ 10%) even for very small $\sqrt{St}$ (e.g., ~ 0.1), suggesting an ever-present "small particle contamination" on an impaction plate intended to catch only larger particles. This phenomenon is not too difficult to understand if the value of St is evaluated according to the ratio of stop distance and the actual particle radial position at the nozzle exit (instead of $D/2$). Thus, the particles closer to the axis would have larger effective value of St and therefore would be expected to impact on the plate. The particles around the nozzle axis should then have very large (effective) St and always impact on the plate regardless their sizes.

When considering the laminar flow field associated with the impinging jet (cf. Fig. 2), the radial component of flow velocity u_r is expected to increase with r starting from zero at r = 0, according to the continuity equation (1), as the jet approaches the plate surface with the axial component u_z decreasing to zero. In the vicinity of

the axis ($r = 0$), u_r diminishes and so does the deflecting flow parallel to the plate surface. Thus, particles around the symmetry axis cannot be deflected but always arrive at the center of impaction plate. As a check, computations are carried out with a reduction of ρ_p from 1000 to 10 kg m^{-3} which effectively reduces $\sqrt{St}$ from 0.124 to 0.0124 for $d_p = 0.5$ μm (at Re = 1132), with results showing $\eta_{0.5} = 0.078$ and $\eta_4 = 0.156$. Hence, the last ten percent of small particles are very difficult to prevent from impacting on the plate. In fact, the characteristic "S" shape deposition efficiency curves often observed experimentally with enhanced small particle impaction had also been commented by Jurcik and Wang (1995), which seem to be consistent with their computational results.

3.2 Tapered Nozzle (with $\phi = 15°$)

Many impactors are designed to have a tapered inlet for practical reasons (cf. Marple and Willeke, 1976). In cascade impactors, the taper half angle is usually larger than 15°. However, the Aerosol Jet® deposition nozzles typically have smaller ϕ for the desire of minimizing deviation of ink droplets from the flow streamlines. Among numerous possibilities, the effect of having a taper section in the nozzle inlet channel on particle deposition pattern is examined here with the taper half angle specified as $\phi = 15°$ (with $D = 1.5$ mm and $D_{in} = 3$ mm). The results are expected to adequately illustrate the basic trends of particle impaction behavior with tapered nozzle configuration.

Table 3 shows the values of computed deposition efficiency η for various $\sqrt{St}$, as Table 2 with the value of S/D labeled as the subscript but for a tapered nozzle with $\phi = 15°$. The value of η is rather insensitive to the change of S/D for the most part, except that η_4 (for $S/D = 4$) becomes noticeably lower than others between $\sqrt{St} = 0.4$ and 0.6. The variation of $\sqrt{St_{50}}$ is also insignificant for different values of S/D with an average of 0.417 and a minimum of 0.405 around $S/D = 1$. Compared with the corresponding values of h in Table 2 for straight nozzle, the tapered nozzle tends to yield steeper slope of the deposition efficiency curve for often desired sharper "cut". This could be a consequence of the aerodynamic focusing effect with the converging flow in tapered channel.

However, the particles flowing adjacent to the wall in a tapering channel can impact and stick on the channel wall due to their inertia. For example, the present computations show that all particles of $d_p = 0.5$ μm and larger ($\sqrt{St} \geq 0.124$) placed within $\delta \sim 15$ μm from the wall at inlet would impact on the nozzle channel wall instead of exiting the nozzle orifice. This translates to about 2.0% of the incoming particles within uniform concentration becoming "wall loss" in the tapered nozzle channel. Such wall loss is shown to increase with increasing $\sqrt{St}$. About 5.9% of the incoming particles would

impact the papered nozzle channel wall for $\sqrt{St} = 1.097$ ($d_p = 5$ μm, $\delta \sim 45$ μm). Therefore, the values of h in Table 3 are calculated based on the fractions of particles actually exiting the nozzle rather than the fractions of incoming particles at inlet, by replacing D_{in} in (11) with $D_{in} - 2\delta$ where the value of δ depends on the particle size (increasing with d_p). To prevent such a wall loss, introducing a co-flowing sheath gas with a flow rate about 10% of the particle-laden mist flow can be practically effective.

Table 3 As Table 2 but for tapered nozzle with $\phi = 15°$. The values of $\sqrt{St_{50}}$ are 0.425, 0.405, 0.411, and 0.427 for S/D = 0.5, 1, 2, and 4, respectively

$\sqrt{St}$	$\eta_{0.5}$	η_1	η_2	η_4
0.124	0.09	0.12	0.12	0.12
0.233	0.12	0.17	0.16	0.16
0.341	0.24	0.29	0.29	0.29
0.395	0.41	0.47	0.45	0.42
0.449	0.84	0.79	0.78	0.65
0.665	1.00	1.00	1.00	1.00
0.881	1.00	1.00	1.00	1.00
1.097	1.00	1.00	1.00	1.00

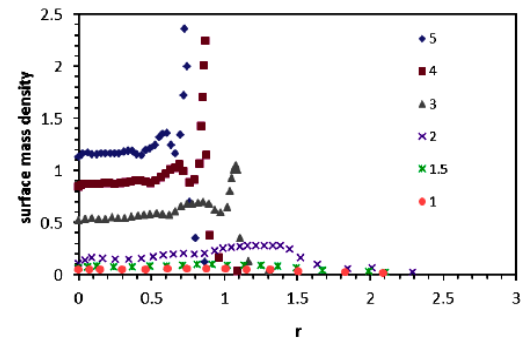**Fig. 5. As in Fig. 3 but for tapered nozzle with $\phi = 15°$.**

As in Fig. 3 but for tapered nozzle with $\phi = 15°$, profiles of the particle mass density $s(r)$ deposited on the impaction plate are shown in Fig. 5 for $d_p = 5, 4, 3, 2, 1.5$ and 1 μm (as labeled). The differences made by the tapering nozzle channel appear to be quite significant, in comparison with Fig. 3. The converging flow in the tapering channel induces the aerodynamic focusing effect that pushes particles inward (cf. Dahneke *et al.*, 1982; Rao *et al.*, 1993), which becomes stronger on larger particles placed further away from the axis (at larger r). As a consequence, a region of concentrated particle deposition appears toward the edge of the circular deposition spot, shown as sharp peaks in Fig. 5 for relatively large particles (which is absent in Fig. 3).
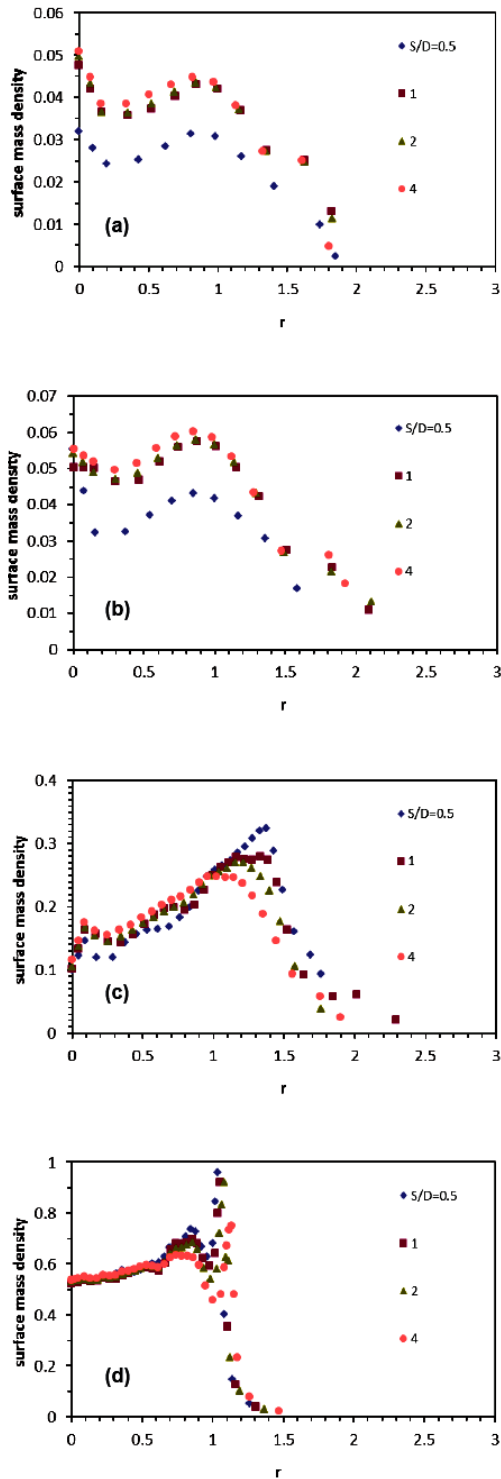
Fig. 6. As in Fig. 4 but for tapered nozzle with $\phi = 15°$.

Another noticeable effect of the tapered nozzle is that the spot radius $\bar{r}$ in Fig. 5 varies more substantially with $\sqrt{St}$ than that for the straight nozzle (shown in Fig. 3), as expected based on the dependence of aerodynamic focusing effect upon particle size. For example, the values of $\bar{r}$ are 0.76, 0.88, 1.09, 1.52, 1.52, and 1.47 for $\sqrt{St}$ = 1.097, 0.881, 0.445, 0.449, 0.341, and 0.233,

respectively (corresponding to the labels 5, 4, 3, 2, 1.5, and 1 in Fig. 5). With decreasing $\sqrt{St}$, the particles tend to flow the outward deflecting gas flow more closely before arriving at the plate, leading to generally increased spot radius $\bar{r}$.

The effect of jet-to-plate distance S/D on particle deposition pattern is shown in Fig. 6, as Fig. 4 but for tapered nozzle with $\phi = 15°$. The profiles of $\sigma(r)$ for small particles, as shown in Fig. 6(a) and (b), with $\sqrt{St}$ = 0.124 and 0.233, have similar shapes for various S/D except that the ones for S/D = 0.5 are relatively lower corresponding to lower h in Table 3. The values of spot radius $\bar{r}$ in Fig. 6(a) for $\sqrt{St}$ = 0.124 are 1.41, 1.61, 1.57, and 1.55, respectively for S/D = 0.5, 1, 2, and 4, while those in Fig. 4(b) for $\sqrt{St}$ = 0.233 are 1.47, 1.47, 1.41, and 1.36.

The profiles in Fig. 6(c) for $\sqrt{St}$ = 0.449 (d_p = 2 µm) show very similar "donut" shape (having a ring of high particle density toward deposition spot edge) to that found experimentally by Sethi and John (1993) for their case of $\sqrt{St}$ = 0.48 (which is the case of smallest $\sqrt{St}$ illustrated in their plots). It exhibits a gradual piling peak toward the edge of the deposition spot. The values of $\bar{r}$ in Fig. 6(c) for $\sqrt{St}$ = 0.449 are 1.52, 1.52, 1.49, and 1.45, respectively for S/D = 0.5, 1, 2, and 4, while those in Fig. 4(d) for $\sqrt{St}$ = 0.665 are 1.08, 1.09, 1.11, and 1.16. The profiles of $\sigma(r)$ for larger $\sqrt{St}$ (> 0.6) also look similar to those illustrated by Sethi and John (1993) except that their experimental data points are spaced a bit too coarse to resolve the narrow peaks toward the spot edge. Such a reasonable comparison with the experimentally measured pattern (Sethi and John, 1993) may serve as an independent validation-verification for the present computational results. The plots (c) and (d) of Fig. 6 show a general trend of reducing the peak particle density with increasing S/D.

3.3 Cases with *Re* = 283

If all the parameters are kept the same except the flow rate Q is reduced to 300 ccm (from its nominal value of 1200 ccm), the value of the jet Reynolds number *Re* becomes 283 (instead of 1132). In this case, the values of $\sqrt{St}$ corresponding to given d_p would become one half of those in Tables 1-3.

Shown in Table 4 are values of the deposition efficiency η versus $\sqrt{St}$ for various particle diameter d_p, as in Table 2 but for *Re* = 283 with ϕ = 15°. Comparing with Table 3 for *Re* = 1132, the values of η corresponding to similar $\sqrt{St}$ are generally lower at *Re* = 283, as expected from thicker viscous boundary layer at reduced *Re*. Unlike the case of *Re* = 1132, the value of $\sqrt{St_{50}}$ at *Re* = 283 in Table 4 increases monotonically with S/D from 0.422 to 0.5. Table 4 suggests a trend of

reduced sharpness of a cut with increasing jet-to-plate distance.

Table 4 As Table 2 but for d_p = 0.5, 1, 2, 3, 4, 5, 6, and 8 μm at *Re* = 283 with ϕ =15°. The values of $\sqrt{St_{50}}$ are 0.422, 0.429, 0.458, and 0.500 for *S/D* = 0.5, 1, 2, and 4, respectively

$\sqrt{St}$	$\eta_{0.5}$	η_1	η_2	η_4
0.062	0.03	0.05	0.05	0.05
0.116	0.04	0.06	0.06	0.05
0.225	0.06	0.09	0.08	0.07
0.332	0.13	0.19	0.17	0.14
0.440	0.57	0.54	0.44	0.32
0.548	0.93	0.89	0.79	0.64
0.656	0.97	0.96	0.92	0.92
0.870	1.00	1.00	1.00	1.00

Similar to Figs. 3 and 5, the particle deposition pattern in terms of σ(*r*) is shown in Fig. 7 for tapered nozzle with ϕ = 15° at *Re* = 283. In contrast to Fig. 5 with the same tapered nozzle, the profiles in Fig. 7 do not show those narrow peaks toward the edge even for particles with relatively large $\sqrt{St}$; they rather appear similar to those profiles in Fig. 3 for the straight nozzle. Interestingly, even the values of spot radius $\bar{r}$ corresponding to similar values of $\sqrt{St}$ in Fig. 7 are fairly comparable to those in Fig. 3 (rather than Fig. 5). For example, corresponding to $\sqrt{St}$ = 0.225 and 0.116 in Fig. 7 we have $\bar{r}$ = 1.19 and 1.24, comparable to 1.24 and 1.21 for $\sqrt{St}$ = 0.233 and 0.124 in Fig. 3 but not around $\bar{r} \sim 1.5$ as in Fig. 5. For larger values of $\sqrt{St}$, e.g., $\sqrt{St}$ = 0.872, 0.656, and 0.440 in Fig. 7 the corresponding values of $\bar{r}$ are 0.76, 0.88, and 1.13, comparable to those in both Fig. 3 and Fig. 5. So, the particle deposition spot size becomes insensitive for $\sqrt{St}$ > 0.4 to the changes of *Re* and ϕ.
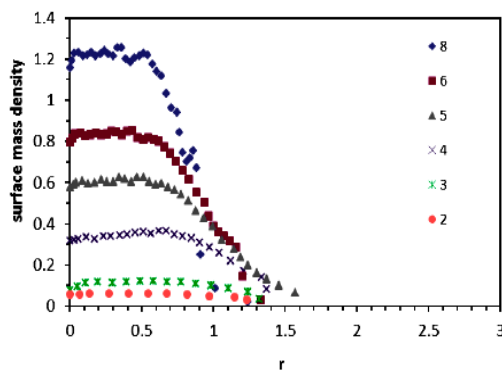

Fig. 7. As in Fig. 5 but for *Re* = 283 and d_p = 8, 6, 5, 4, 3, and 2 μm.

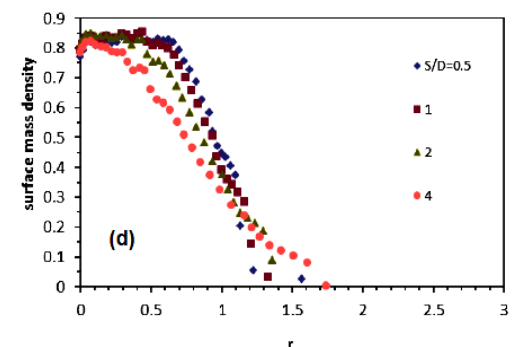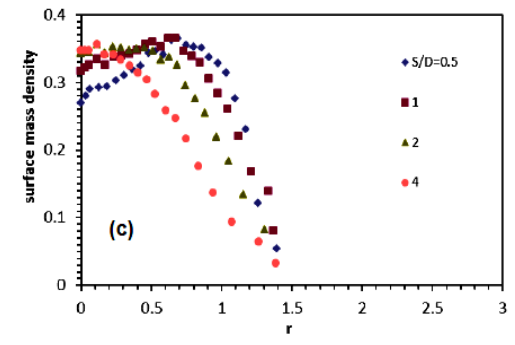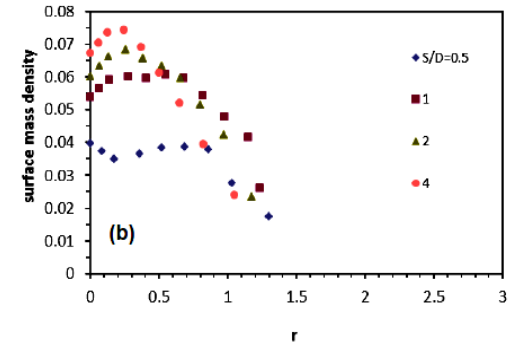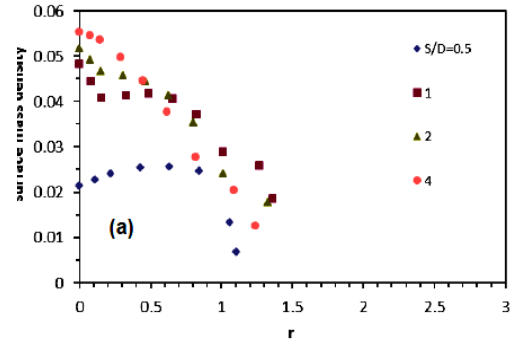**Fig. 8. As in Fig. 6 but for *Re* = 283 with ϕ =15° and d_p = 1, 2, 4, and 6 μm.**

The effect of jet-to-plate distance *S/D* is shown in Fig. 8 for *Re* = 283 with ϕ = 15°, as in Figs. 4 and 6 but with d_p = 1, 2, 4, and 6 μm. In contrast to those in Figs. 4 and 6 with similar values of $\sqrt{St}$, the particle deposition pattern in Fig. 8 varies much more significantly, which appears also consistent

with the deposition efficiency data in Table 4. The value of $\eta_{0.5}$ for small $\sqrt{St}$ is obviously lower in plots (a) and (b) of Fig. 8 than the corresponding ones in Figs. 4 and 6. The trend of decreasing η with increasing S/D is clearly reflected in Fig. 8(c) with shrinking $\bar{r}$ (= 1.19, 1.13, 1.01, and 0.81 for S/D = 0.5, 1, 2, and 4, respectively) but comparable peak value of σ. Despite the differences of $\sigma(r)$ between that for S/D = 2 (with $\bar{r}$ = 0.84) and S/D = 4 ($\bar{r}$ = 0.79) in Fig. 8(d), both curves have a comparable value of $\bar{r} \sim 0.8$ and the same value of η in Table 4. Such a feature of gradual declining $\sigma(r)$ without a clearly defined edge becomes the common pattern also exhibited with cases of straight nozzle (ϕ = 0) at Re = 283 (not shown here with graphs). Reducing particle density near the edge of deposition spot with increasing S/D can readily be observed in plots (c) and (d) of Fig. 8 when $St > St_{50}$.

If straight nozzle is used with a jet flow at Re = 283, the profiles of σ (r) become more or less like a Gaussian function similar to that in Fig. 8(d) for S/D = 4, without a clearly defined edge. This is in sharp contrast to those for Re = 1132 with a flat center in Fig. 3.

Relatively speaking, the tapered nozzle tends to deposit more particles toward the deposition spot edge than the straight nozzle. Reducing the value of Re generally leads to reduced particle density toward the deposition spot edge, with profiles of particle density $\sigma(r)$ exhibiting more gradual declining slopes as the radial distance increases away from the deposition center on the impaction plate.

3.4 Deposition Efficiency η Versus $\sqrt{St}$

The study of particle deposition cannot be completed without an examination of the deposition efficiency versus particle size. As given in Tables 2 and 3 for Re = 1132, the values of η at a given $\sqrt{St}$ are fairly insensitive to the (normalized) jet-to-plate distance S/D, except for straight nozzle with S/D = 0.5 with noticeably lower η for $\sqrt{St}$ < 0.4, and for tapered nozzle with S/D = 4 with lower η within a narrow interval around $\sqrt{St}$ = 0.47, between 0.42 and 0.52. The straight nozzle configuration is not very sensitive to the S/D variation when S/D > 1, whereas the tapered nozzle configuration insensitive to the S/D variation when S/D < 2.

At Re = 283, however, the value of η for a given $\sqrt{St}$ seems to change substantially with the variation of S/D, especially between $\sqrt{St}$ = 0.4 and 0.6 as shown in Fig. 9(a). A consistent trend can be seen with noticeably lower η_4 for relatively larger $\sqrt{St}$ while having lower $\eta_{0.5}$ for smaller and diminishing $\sqrt{St}$, as also apparent in Tables 2-4. The general trend of lower η with smaller Re at a given $\sqrt{St}$ is shown in Fig. 9(b), for both straight and tapered nozzles (with S/D = 1). It also illustrates the fact that tapered nozzles yield

relatively sharper cut in terms of η versus $\sqrt{St}$, i.e., with lower η for $\sqrt{St}$ < $\sqrt{St_{50}}$ and higher η for larger $\sqrt{St}$, than the straight nozzles.
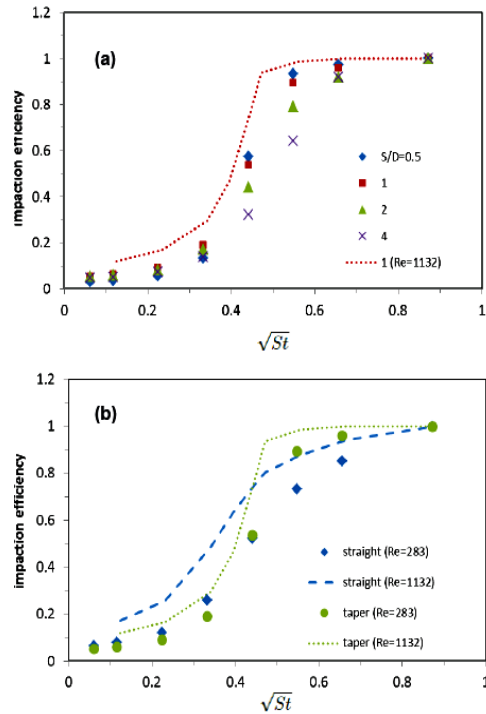

Fig. 9. Particle deposition efficiency η versus $\sqrt{St}$. Plot (a) is for tapered nozzle with ϕ =15° at Re = 283 with S/D = 0.5, 1, 2, and 4, and at Re = 1132 with S/D = 1 as reference; plot (b) for comparison of cases with straight and tapered nozzles at Re = 283 and 1132 for S/D = 1.

Table 5 As Table 4 but for straight nozzle with ϕ =0. The values of $\sqrt{St_{50}}$ are 0.425, 0.431, 0.459, and 0.505 for S/D = 0.5, 1, 2, and 4, respectively

$\sqrt{St}$	$\eta_{0.5}$	η_1	η_2	η_4
0.062	0.05	0.07	0.07	0.05
0.116	0.05	0.08	0.07	0.06
0.225	0.09	0.12	0.11	0.09
0.332	0.23	0.26	0.22	0.18
0.440	0.54	0.52	0.47	0.36
0.548	0.78	0.73	0.67	0.59
0.656	0.88	0.85	0.83	0.80
0.870	0.94	1.00	1.00	1.00

For completeness, values of η with the straight nozzle (ϕ = 0) at Re = 283 for S/D = 0.5, 1, 2, and 4 are computed and shown in Table 5. Comparing with those in Table 4 for tapered nozzle, the range of variation in η with S/D in Table 5 is general

smaller. In other words, the deposition efficiency of straight nozzle is less sensitive to the *S/D* variation than that of tapered nozzle.

With regard to the small particle contamination, reducing *Re* seems to help as indicated in Fig. 9 as well as Tables 2-4. Yet still, the value of η does not become zero with diminishing $\sqrt{St}$, for the same reason discussed at the end of subsection 3.1. At Re = 283, about 5% of small particles with $\sqrt{St} \sim 0.05$ still impact on the plate without being deflected by the radially diverging "wall jet" flow along the pate surface. The small particle contamination may be reduced somewhat by optimizing the impactor design, but it may never be eliminated completely in the inertial impactor.

4. CONCLUSIONS

Investigation of particle deposition pattern on the impaction plate of an inertial impactor is carried out numerically using a lagrangian solver implemented within the OpenFOAM® framework. Various effects of the impactor configuration, such as the jet-to-plate distance, taper angle of the nozzle channel, etc., are examined with discussion of physical implications, for gaining insights into the ink deposition behavior during Aerosol Jet® printing.

At *Re* = 1132 (where *Re* denotes the jet Reynolds number), the particle deposition patterns corresponding to different values of $\sqrt{St}$ (where St denotes the particle Stokes number) with the straight nozzle (where the taper half angle ϕ = 0) are mostly as expected, having a relatively flat center and quickly declining particle density toward the edge of the deposition spot. But with a tapered nozzle (having ϕ = 15º), the deposited particles form a high density ring near the edge of the deposition spot especially for $St > St_{50}$, due to the relatively strong aerodynamic focusing effect on particles further away from the symmetry axis. The tapered nozzle tends to deposit particles in larger circular patterns (with larger spot radius) than the straight nozzle for the same value of *St*, and its deposition spot radius seems to be more sensitive to the variation of *St* (expected based on the dependence of aerodynamic focusing effect upon particle size). A general trend of reduced particle density peak near the deposition spot edge is shown with increasing the jet-to-plate distance.

By reducing *Re* from 1132 to 283, particles deposited with the same tapered nozzle (having ϕ = 15º) do not seem to form the high density peak toward the deposition spot edge. Similar to the straight nozzle case of *Re* = 283, reducing *Re* tends to reduce the particle density around the deposition spot edge more significantly than that closer to the center. The similar trend is also shown by increasing the jet-to-plate distance.

A closer inspection of the particle deposition efficiency η reveals the fact that particles around the jet center always impact on the plate no matter how small they are. The value of η does not approach zero with a substantial (e.g., orders of magnitude) reduction of the value of *St*. This should not be difficult to understand based on the impinging jet flow structure. The particles along the jet center (*r* ~ 0) will not be readily deflected by the bending gas flow streamlines, with diminishing radial velocity component at the center of the stagnation zone. Such a "small particle contamination" phenomenon, typically amounts to ~10% small particles with $\sqrt{St}$ < 0.1 at *Re* ~ 1000 and ~5% at *Re* ~ 300, may not be negligible in data analysis with inertial impactor measurement.

REFERENCES

Andersen, A. A. (1966). A sampler for respiratory health hazard assessment. *Am. Ind. Hyg. Assoc. J.* 27(2), 160-165.

Christenson, K. K., J. A. Paulsen, M. J. Renn, K. McDonald, and J. Bourassa (2011). Direct printing of circuit boards using Aerosol Jet®. *Proc. NIP 27 Digital Fabric.* 433-436.

Dahneke, B., J. Hoover and Y. S. Cheng (1982). Similarity theory for aerosol beams. *J. Colloid Interf. Sci.* 87(1), 167-179.

Feng, J. Q. (2015). Sessile drop deformations under an impinging jet. *Theor. Comput. Fluid Dyn.* 29, 277-290.

Friedlander, S. K. (1977). *Smoke, Dust and Haze, Fundamentals of Aerosol Behavior.* John Wiley & Sons, New York.

Fuchs, N. A. (1964). *The Mechanics of Aerosols.* Pergamon Press, New York.

Hedges, W. M., B. King and M. Renn (2007). Direct writing for advanced electronics packaging.

Hering, S. V. (1995). Impactors, cyclones, and other inertial and gravitational collectors. In Cohen, B., Hering, S. V. (Eds) *Air Sampling Instruments for Evaluation of Atmospheric Contaminants*, 8th Edition, American Conference of Governmental Industrial Hygienists, Cincinnati, OH, 279-322.

Huang, C. H. and C. J. Tsai (2001). Effect of gravity on particle collection efficiency of inertial impactors. *J. Aerosol Sci.* 32, 375-387.

Jurcik, B. and H. C. Wang (1995). On the shape of impactor efficiency curves. *J. Aerosol Sci.* 26(7), 1139-1147.

Kahn, B. E. (2007). The M³D aerosol jet system, an alternative to inkjet printing for printed

electronics. *Organic and Printed Electronics* 1, 14-17.

Marple, V. A. (1970). *A Fundamental Study of Inertial Impactors*. Ph.D. thesis, University of Minnesota, Minneapolis.

Marple, V. A. and B. Y. H. Liu (1974). Characteristics of laminar jet impactors. *Environmental Sci. Technol.* 8, 648-654.

Marple, V. A. and B. Y. H. Liu (1975). On the fluid flow and aerosol impaction in inertial impactors. *J. Colloid Interf. Sci.* 53, 31-34.

Marple, V. A. and K. Willeke (1976). Impactor design. *Atmos. Environ.* 10, 891-896.

May, K. R. (1975). Aerosol impaction jets. *J. Aerosol Sci.* 6, 603-411.

Paulsen, J. A., M. Renn, K. Christenson and R. Plourde (2012). Printing conformal electronics on 3D structures with Aerosol Jet technology. In *Future of Instrumentation International Workshop* (FIIW

Ranz, W. E. and J. B. Wong (1952). Impaction of dust and smoke particles on surface and body collectors. *Industrial and Engineering Chemistry* 44, 1371-1381.

Rao, N. P., J. Navascues and J. F. de la Mora (1993). Aerodynamic focusing of particles in viscous jets. *J. Aerosol Sci.* 24, 879-892.

Renn, M. J. (2006). Direct Write^{TM} system. *U. S. Patent* 7,108,894 B2.

Renn, M. J. (2007). Direct Write^{TM} system. *U. S. Patent* 7,270,844 B2.

Renn, M. J., B. H. King, M. Essien, G. J. Marquez, M. G. Giridharan and J. C. Shen (2009). Apparatuses and methods for maskless mesoscale material deposition. *U. S. Patent* 7, 485, 345 B2.

Renn, M. J., M. Essien, B. H. King and J. A. Paulsen (2010). Aerodynamic jetting of aerosolized fluids for fabrication of passive structures. *U. S. Patent* 7,674,671 B2.

Schiller, L. and A. Naumann (1933). Uber die grundlegenden Berechnungen bei der Schwekraftaubereitung. *Zeitschrift des Vereines Deutsher Ingenieure* 77(12), 318-320.

Sethi, V. and W. John (1993). Particle impaction patterns from a circular jet. *Aerosol Sci. Technol.* 18(1), 1-10.

Zollmer, V., M. Muller, M. Renn, M. Busse, I. Wirth, D. Codlinski and M. Kardos (2006). Printing with aerosols: A maskless deposition technique allows high definition printing of a variety of functional materials. *Euro. Coating J.* 07-08, 46-55.